



Synthesis of 1D nanorod and 2D nanoflake mixed structures of nickel cobaltite: an efficient diffusion-controlled electrode material for asymmetric supercapacitor application

M. Sathiyaseelan¹ · Lakshmi Kunhikrishnan² · P. Jacqueline Rosy³ · G. Sivashanmugam⁴ · B. Preethi⁵ 

Received: 22 December 2023 / Accepted: 6 March 2024 / Published online: 1 April 2024
© The Author(s), under exclusive licence to Springer-Verlag GmbH, DE part of Springer Nature 2024

Abstract

The intercalation pseudocapacitance mechanism holds the potential to significantly narrow the gap between supercapacitors and lithium-ion batteries, particularly in terms of energy density and power density properties. Herein, 1D nanorod and 2D nanoflake mixed structures of nickel cobaltite (NiCo_2O_4) were prepared for asymmetric supercapacitor application. For comparison, the NiO and Co_3O_4 materials were also prepared, and examined their supercapacitor properties. The NiCo_2O_4 store charges through the diffusion-controlled process and delivers the specific capacity of 347 C g^{-1} (694 F g^{-1}) at 1 A g^{-1} and it withstands 96% of initial capacity after 5000 cycles at a current density of 10 A g^{-1} . Furthermore, the asymmetric supercapacitor device ($\text{NiCo}_2\text{O}_4//\text{AC}$) exhibits the specific capacity of 141 C g^{-1} (88 F g^{-1}) at 1 A g^{-1} , with an excellent energy and power density of 31.3 Wh kg^{-1} and 800 W kg^{-1} respectively. The device retained 86% of its initial capacity after 5000 GCD cycles at 10 A g^{-1} . Therefore, the 1D/2D mixed morphologies with diffusion-controlled charge storage process are guaranteed to achieve superior electrochemical performance.

Keywords 1D/2D morphology · NiCo_2O_4 · Diffusion -controlled · Supercapacitors · Energy storage

M. Sathiyaseelan and Lakshmi Kunhikrishnan equally contributed to this work.

✉ G. Sivashanmugam
sivashanmugam.gss@gmail.com

✉ B. Preethi
preethichemistry20@gmail.com

¹ Department of Chemistry, Swami Dayananda College of Arts and Science, (Affiliated to Bharathidasan University), Manjakkudi, Tamil Nadu 612610, India

² Department of Chemistry, Anand Institute of Higher Technology, Chennai, Tamilnadu 603103, India

³ Department of Chemistry, IFET College of Engineering (Autonomous), Villupuram, Tamilnadu 605108, India

⁴ Department of Chemistry, Peri Institute of Technology, Chennai, Tamilnadu 600048, India

⁵ Department of Chemistry, Karpagam Academy of Higher Education, Coimbatore, Tamilnadu 641021, India

1 Introduction

Over the past few years, supercapacitors have garnered significant attention as energy storage solutions for applications demanding rapid charge/discharge characteristics. These applications encompass high-power electronic devices and electric vehicles. Supercapacitors deliver superior power density while maintaining an extended cycling lifespan compared to traditional batteries. Furthermore, they can store a greater amount of energy when compared to traditional capacitors [1, 2]. The ion adsorption/desorption or fast redox reaction process are the two energy storage mechanisms that occur in Electric double-layer capacitors (EDLC) and pseudocapacitors respectively [3, 4]. Regrettably, the limited specific capacitance of EDLCs falls short of meeting the ever-increasing demand for peak-power support in electric vehicles and similar applications. Consequently, there has been a burgeoning interest in the adoption of pseudocapacitive materials in supercapacitors. This surge in interest has been driven by the significant increase in energy density resulting from Faradaic reactions, which is at least one order of magnitude greater than that achieved by EDLCs [5].

Further, the Pseudocapacitors store charges using three different charge storage mechanisms: underpotential deposition, redox pseudocapacitance, and intercalation pseudocapacitance [6]. The underpotential deposition charge storage mechanism takes place when a metal electrode is polarized at a potential below the presumed value for a redox reaction. This phenomenon induces electrochemical adsorption and desorption of ions on the electrode's surface, giving rise to pseudocapacitance [7]. Redox pseudocapacitance encompasses electron transfer between the electrode and the electrolyte, which plays a significant role in driving the pseudocapacitive characteristics of the device [8]. Conversely, intercalation pseudocapacitance relies on materials capable of reversibly intercalating ions from the electrolyte into their crystal structure. This intercalation and de-intercalation process (battery-like charge storage mechanism), occurring during charging and discharging cycles, greatly enhances the overall pseudocapacitive performance of the device. By way of comparison, Supercapacitors, which store energy through either EDLC or surface Faradaic redox pseudocapacitance, exhibit remarkable rate performance. However, it's important to note that their energy density still lags significantly behind that of lithium-ion batteries. On the other hand, the intercalation supercapacitors store energy through a battery-like process, while still exhibiting rapid reaction kinetics like a supercapacitor. This intercalation pseudocapacitance has the potential to substantially bridge the gap between supercapacitors and lithium-ion batteries in terms of energy density and power density. This creates a fresh opportunity for the advancement of energy storage systems that can offer both high energy density and power density simultaneously [9].

To attain high energy density and power density features, it is essential to design the electrodes in a way that incorporates a substantial quantity of electroactive sites and facilitates high rates of transport for both electrolyte ions and electrons. These elements work in tandem during the Faradaic reactions, contributing to enhanced performance. This can be accomplished by preparing the high surface area electroactive materials with various morphologies, resulting in a significant increase in surface area, improved electrical conductivity, and enhanced ion transport capabilities. Notably, one-dimensional (1D) and two-dimensional (2D) nanostructures have gained significant recognition because of their unique structural characteristics and inherent attributes [10, 11]. Specifically, 1D and 2D nanostructures offer an abundance of surface-active sites, effectively shortening the routes for electrolyte ion movement during electrochemical reactions. This leads to accelerated charge/discharge rates and an expanded electrode/electrolyte interface. Furthermore, 2D nanostructures possess impressive planar electronic conductivity, while their reduced thickness enhances their electrochemical reactivity. In addition, the

2D morphologies experienced the spacer effect during the cyclic stability analysis due to the restocking factor. The 1D and 2D morphologies mixed morphologies could overcome these drawbacks to enhance electrochemical performance [12, 13]. Still, various nanomaterials with 1D and 2D morphologies are used to prepare the electroactive materials for supercapacitors [14, 15].

Here, we develop 1D and 2D mixed morphologies of NiCo_2O_4 material through the hydrothermal method for asymmetric supercapacitor application. For comparison, the individual components such as NiO and Co_3O_4 were also prepared and examined its electrochemical properties. The NiCo_2O_4 material with various morphologies was utilized as supercapacitor electrodes previously [16, 17]. In this work, we extend the intercalation pseudocapacitance-based NiCo_2O_4 material, which is attained through the preparation of mixed morphologies with 1D and 2D nanostructures. The surface-controlled and diffusion-controlled charge storage mechanism is analyzed in detail for various scan rates in supercapacitor analysis. As stated above, the materials follow the intercalation-pseudocapacitor behavior due to these unique mixed morphologies. Asymmetric device studies were also performed for NiCo_2O_4 material and provided high energy and power density characteristics due to the diffusion-controlled properties. As a result, producing electrode materials in the form of 1D and 2D nanostructured material enhances the desirable supercapacitor properties.

2 Experimental section

2.1 Materials

All reagents are used in their pure form without any further purification. The Nickel nitrate hexahydrate ($\text{Ni}(\text{NO}_3)_2 \cdot 6\text{H}_2\text{O}$), cobalt nitrate hexahydrate ($\text{Co}(\text{NO}_3)_2 \cdot 6\text{H}_2\text{O}$), poly(vinylidene fluoride) (PVDF), and carbon black, were bought from Sigma Aldrich. Additionally, ethanol, urea, diethylamine, and N-methyl-2-pyrrolidone (NMP) were purchased from SRL (India). Furthermore, nickel foil (0.025 mm thickness), polyvinyl alcohol (PVA) (Molecular weight- 88,000–97,000), and N-methyl-2-pyrrolidone (NMP), were procured from Alfa aesar. Throughout the preparation and electrochemical studies, deionized (DI) water was employed exclusively.

2.2 Material synthesis

For the synthesis of NiCo_2O_4 material, 0.02 M $\text{Ni}(\text{NO}_3)_2 \cdot 6\text{H}_2\text{O}$ and 0.04 M $\text{Co}(\text{NO}_3)_2 \cdot 6\text{H}_2\text{O}$ were dissolved into 70 mL of DI water and subjected to stirring for 20 min. Subsequently, 0.2 M of urea was added, followed by an additional 10 min of stirring. Lastly, 5 mL of

diethylamine was gradually introduced into the solution, and stirring was continued for another 10 min. The resulting solution was subsequently transferred to a 100 mL Teflon-lined stainless-steel autoclave and maintained at 150 °C for a duration of 15 h. After attaining room temperature, the resultant precipitate underwent three cycles of cleaning through centrifugation with various solvents such as ethanol, water, and acetone respectively. The resultant material was then subjected to drying in a vacuum oven at 70 °C for 8 h, followed by calcination at 350 °C for 5 h. The same procedure was repeated for the synthesis of NiO and Co₃O₄ materials.

2.3 Material characterizations

The X-ray diffraction (XRD) analyses were done in a Bruker AXS (D8 Discover with GADDS) within 2θ values from 20 to 80° with Cu-Kα radiation ($\lambda = 0.154060$ nm, 30 mA and 40 kV) and X-ray photoelectron spectroscopic (XPS) analysis was done using Ulvac-PHI (PHI Quantera-II) instrument. The Fourier-transform infrared (FTIR) spectroscopic analyses were evaluated using Agilent Cary 670 spectrometer with wavelengths from 4000 to 400 cm⁻¹. The morphological images were recorded by scanning electron microscopy (SEM; Zeiss Ultra Plus) and high-resolution transmission electron microscopy (HRTEM; Techni G2S-TWIN, FEI).

2.4 Electrochemical characterizations

For both three-electrode electrochemical cells and device analysis, the same procedure was followed for the fabrication of electrodes. The active material, carbon black, and polyvinylidene fluoride (PVDF) (80:10:10 ratio) were taken in the mortar pestle and made a slurry with N-methyl-2-pyrrolidone solvent. This slurry was then brush-coated onto the Ni-foam current collector and subsequently dried in a vacuum oven at 60 °C for 12 h. The weight of the active electrode materials was 0.004 g. The obtained electrode served as the working electrode for evaluating the supercapacitor properties. The platinum foil and Ag/AgCl electrodes were used as counter and reference electrodes respectively. A 6 M KOH was served as an electrolyte. All electrochemical assessments were carried out using a Biologic instrument. The asymmetric supercapacitor (ASC) device was fabricated using an activated carbon anode and a NiCo₂O₄ cathode with a PVA/KOH-soaked Whatman filter paper separator. The cyclic voltammetry (CV), Galvanostatic charge/discharge (GCD), and electrochemical impedance spectroscopic (EIS) techniques were utilized for evaluating the supercapacitor properties.

3 Results and discussion

To determine the crystal structure of the NiO, Co₃O₄, and NiCo₂O₄ materials, XRD was recorded and depicted in Fig. 1. The XRD spectra (Fig. 1a) of the NiO material show the diffraction peaks at 2θ values of 37.2, 43.2, 62.8, 75.4, and 79.4° are matched with the (111), (200), (220), (311) and (222) planes of cubic structured NiO phase which more comparable with the JCPDS card No.-01-071-1179 [18]. The XRD spectrum of Co₃O₄ material (Fig. 1b) shows the peak at 2θ = 31.2, 36.8, 38.5, 44.8, 55.6, 59.4, 65.2, 68.6, 74.1, 77.3, and 78.4° are corresponds to (220), (311), (222), (400), (422), (511), (440), (531), (620), (533), and (622) planes of cubic Co₃O₄ phase (JCPDS card no.-42-1467) [19]. Figure 1c shows the XRD spectra of the NiCo₂O₄ material, consist of 2θ peaks at 31.1, 36.6, 38.4, 44.6, 55.4, 59.1, 64.9, 68.3, and 77.5°, are matches to (220), (311), (222), (400), (422), (511), (440), (531), and (533), planes of cubic NiCo₂O₄ phase (JCPDS card no.-20-0781) [20].

Furthermore, there are no additional peaks observed after the hydrothermal process for the formation of NiO, Co₃O₄, and NiCo₂O₄ materials and the subsequent calcination, which indicates the high phase purity of synthesized materials. All the materials provide very shape diffraction patterns, confirming the high crystalline nature of the corresponding materials. The XRD result, chemical composition, and oxidation state of the NiCo₂O₄ material are further verified by the XPS analysis. The survey spectrum of the NiCo₂O₄ material (Fig. 2a) consists of Ni 2p, Co 2p, and O 1s peaks, which confirms the formation of NiCo₂O₄ material. Figure 2b shows the core-level spectra of Ni 2p, which consist of Ni 2p_{3/2} and Ni 2p_{1/2} peaks at 854.3 and 872.4 eV respectively. The Gaussian fitted core level spectra show the peaks at 853.1 and 871.1 eV are ascribed to Ni²⁺, whereas the peaks at 854.9 and 873.4 eV are due to Ni³⁺ oxidation states, along with their two satellite peaks at 861.1 and 878.6 eV respectively [21]. The deconvolution of the Co 2p peaks reveals two spin-orbit doublets, a distinctive feature indicative of Co³⁺ and Co²⁺ ions. Further, the spectra show the peaks at 780.7 and 796.5 eV correspond to Co²⁺ ions, while 778.9 and 794.4 eV indicate Co³⁺ ions along with two satellite peaks at 788.8 and 805.1 eV respectively [22].

The deconvoluted O 1s spectrum consists of three peaks at 530.3, 531.4, and 532.4 eV relating to metal–oxygen binding, hydroxyl group from the atmosphere, and chemisorbed water molecules respectively [23]. The XRD and XPS results confirmed the successful formation of NiCo₂O₄ material in the present work.

The morphological analysis of the NiO, Co₃O₄, and NiCo₂O₄ materials was conducted through SEM analysis,

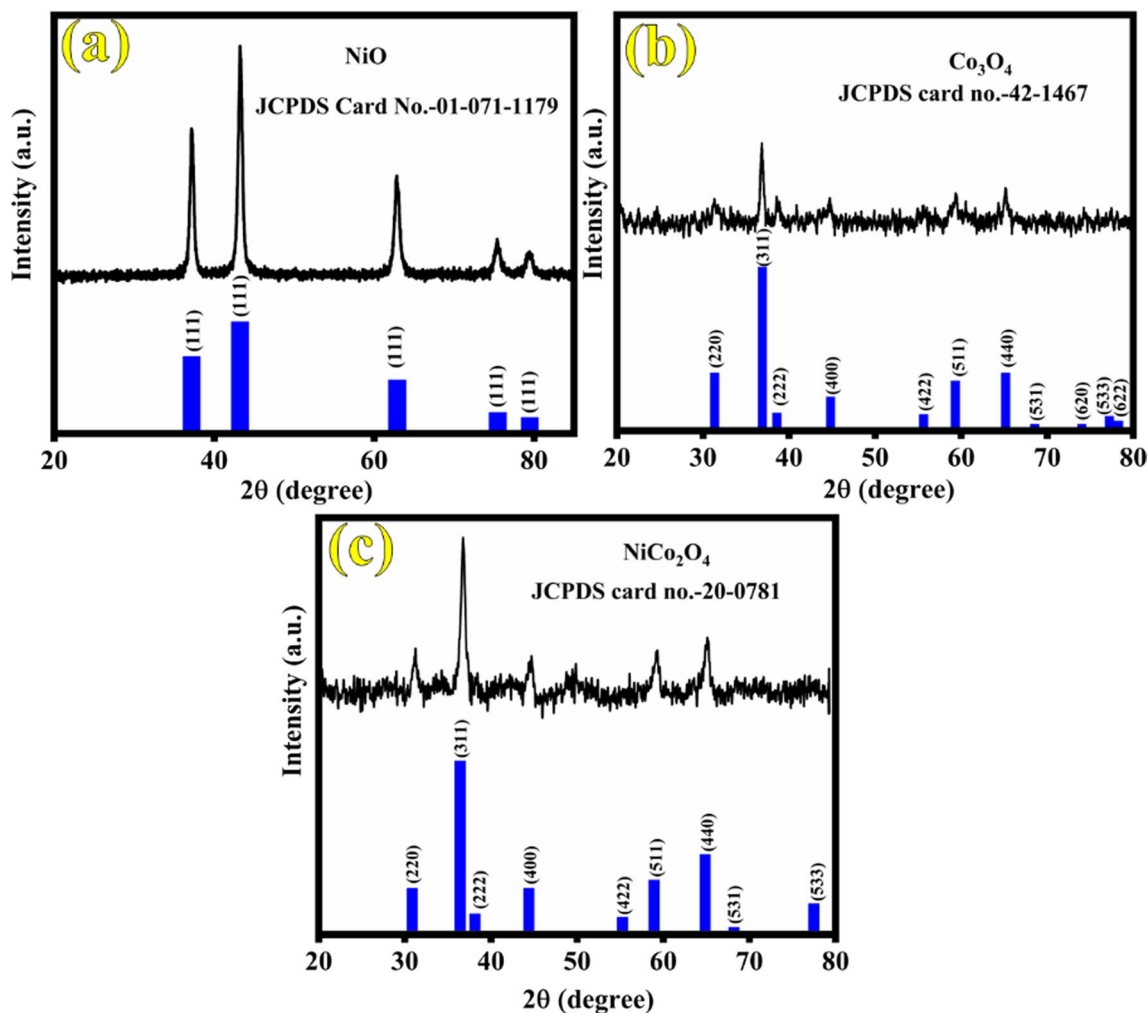


Fig. 1 XRD analysis **a** NiO, **b** Co_3O_4 , and **c** NiCo_2O_4 material

as illustrated in Fig. 3. The SEM images of NiO (Fig. 3a, b) depict predominantly micro-sized particles, although it is worth noting that some nanoparticles are also discernible alongside these micro-sized particles. The SEM images (Fig. 3c, d) of the Co_3O_4 material reveal a nanorod structure. Fascinatingly, the Co_3O_4 nanoparticles are also formed, and it is perfectly visible in the SEM images. Moreover, the SEM images of NiCo_2O_4 (Fig. 3e, f) show the 1 D nanorod and thin 2 D nanoflake structure. The size of the nanorod is 30 ± 10 nm and its lengths span several micrometers.

To understand more clearly, TEM analysis was done for NiCo_2O_4 materials as shown in Fig. 4a, b. The TEM images perfectly show both 1 D nanorods and thin 2 D nanoflake structures. The size of the nanoflake structure is 80 ± 10 nm. The fringe pattern in Fig. 4c shows the d-spacing values of 0.24 and 0.14 nm, which corresponds to (311) and (440) planes of the cubic NiCo_2O_4 phase and it is more comparable with the XRD results. In Fig. 4d, the selected area

electron diffraction pattern is presented, displaying distinct diffraction rings that signify the characteristic polycrystalline nature of the NiCo_2O_4 material. The morphological analytic results confirmed that the NiCo_2O_4 mate contains both 1 D nanorod and thin 2 D nanoflake mixed morphologies.

The reaction mechanism for the synthesis of NiO, Co_3O_4 , and NiCo_2O_4 materials is explained below: At first, the urea and diethylamine generate OH^- ions during the hydrolysis process when it dissolved in DI water. The reaction mechanism for the synthesis of NiO, Co_3O_4 , and NiCo_2O_4 materials is elucidated as follows: Initially, when urea (Equations S1–S2) and diethylamine (Equations S3) dissolve in DI water, they generate OH^- ions [23]. The surplus OH^- ions engage in a reaction with metal ions, leading to the formation of metal hydroxide as an intermediate product. The metal oxides are formed after the calcination of these intermediate products. The formation reaction mechanism for NiO (Equations S4–S5) [24] and Co_3O_4 material (Equations S6–S7) [25] are provided in the supplementary information.

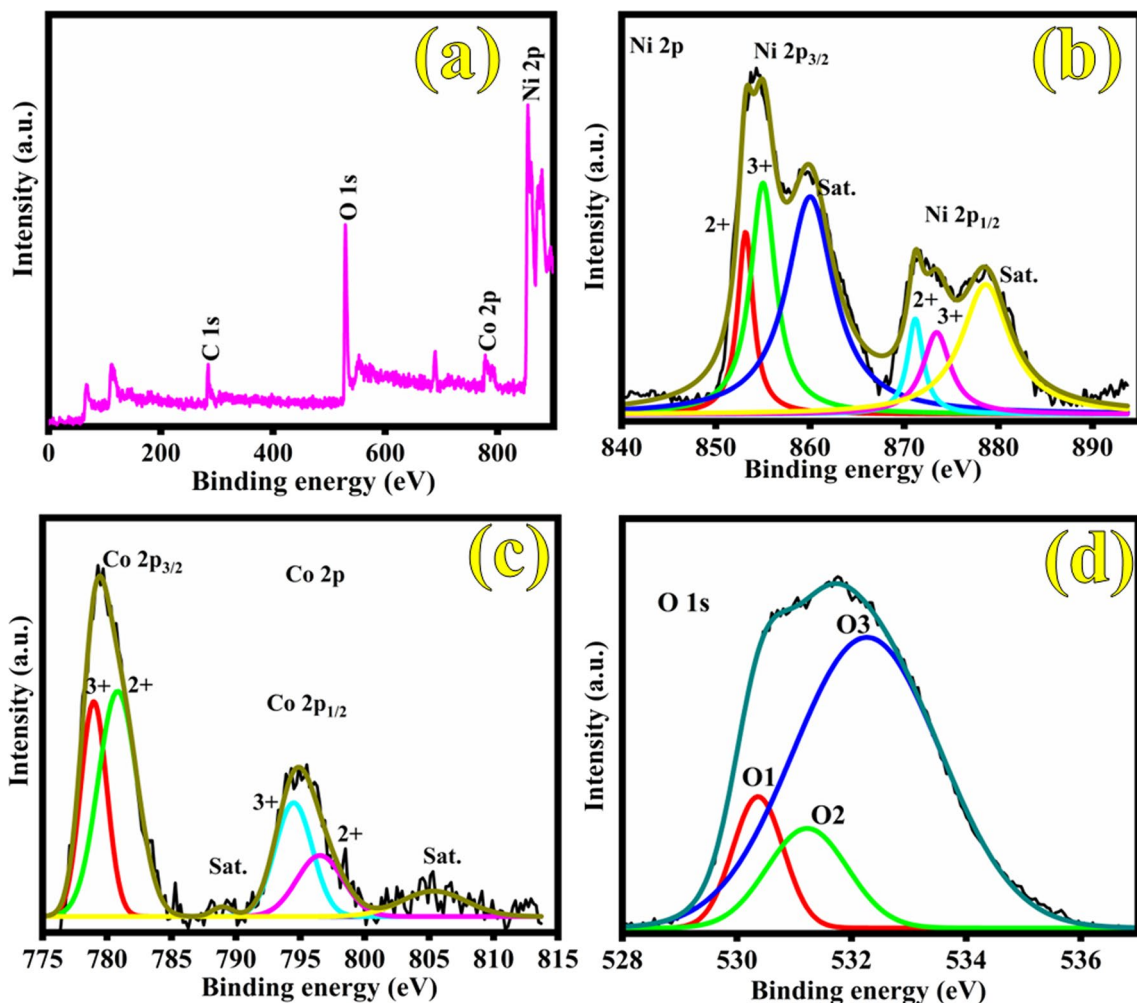
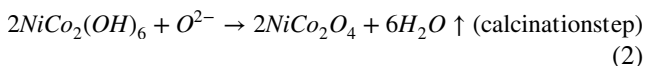


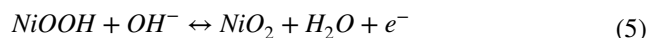
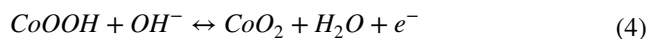
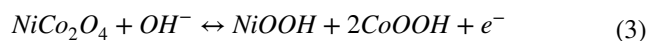
Fig. 2 XPS spectra of NiCo₂O₄ material. a Survey spectra, b Ni 2p, c Co 2p and d O 1 s

Formation of NiCo₂O₄ material (Eqs. 1–2) [26]



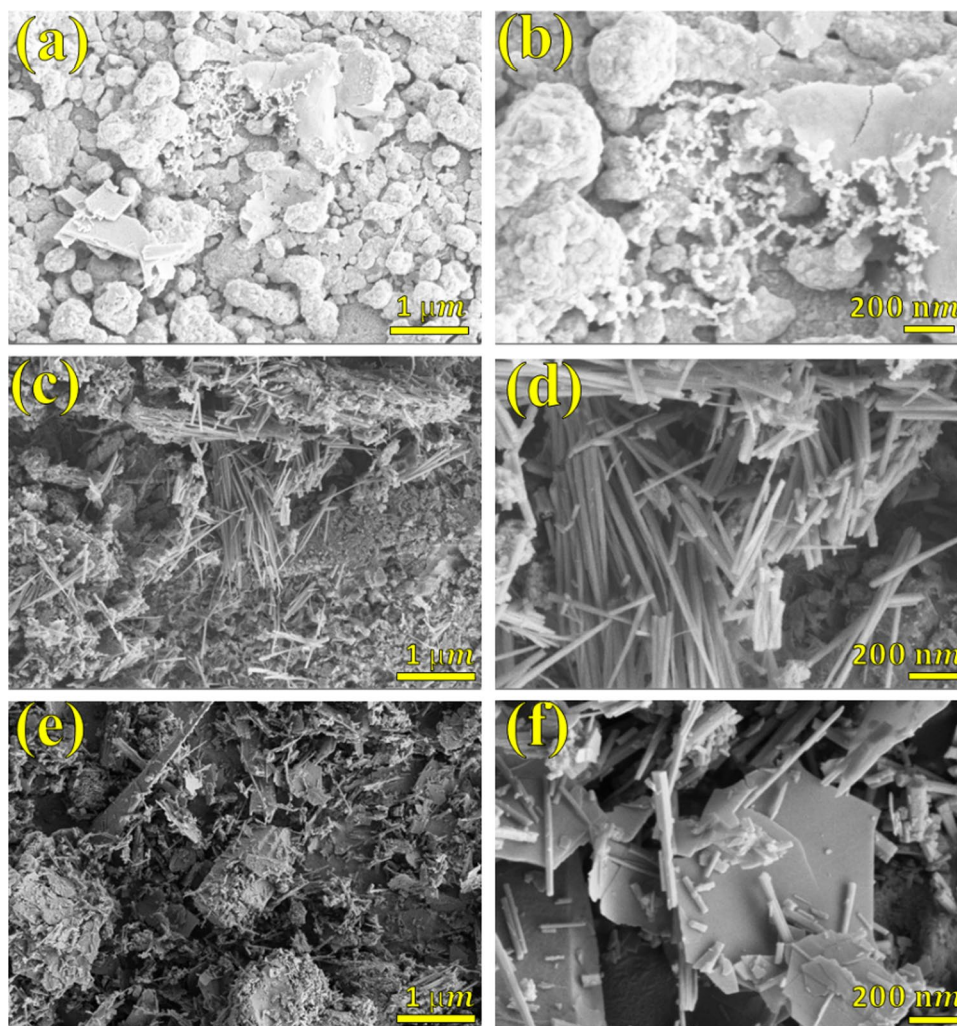
Cyclic voltammetry (CV) galvanostatic charge/discharge (GCD) and electrochemical impedance spectroscopic experiments were carried out using a three-electrode setup to assess the electrochemical characteristics of the NiO, Co₃O₄, and NiCo₂O₄ electrode materials. Figure 5a–c displays the CV profiles of the NiO, Co₃O₄, and NiCo₂O₄ electrodes respectively, at various scan rates, ranging from 5 to 10 mV s⁻¹ in 6 M KOH electrolyte. These CV curves share a common shape and feature a series of prominent redox peaks, suggesting that the primary contribution to specific capacitance arises from rapid and reversible electrochemical redox reactions. This observation highlights that the electrochemical

capacitance of all electrodes differs from the electric double-layer capacitance, which is typically characterized by nearly rectangular CV curves. The appearance of this pair of peaks is predominantly attributed to Faradaic redox reactions associated with M–O/M–O–OH (where M represents Ni or Co). The NiO [27] and Co₃O₄ [25] electrode materials changed into hydroxides (NiOOH and CoOOH respectively) after the reaction with OH⁻ ions from the alkali electrolytes [28]. Also, the same reaction is occurred in NiCo₂O₄ material, which explained using Eqs. (3–5) [29];



The high-power properties of electrodes become evident when examining their voltammetric response at different

Fig. 3 SEM analysis **a, b** NiO, **c, d** Co₃O₄, and **e, f** NiCo₂O₄ material



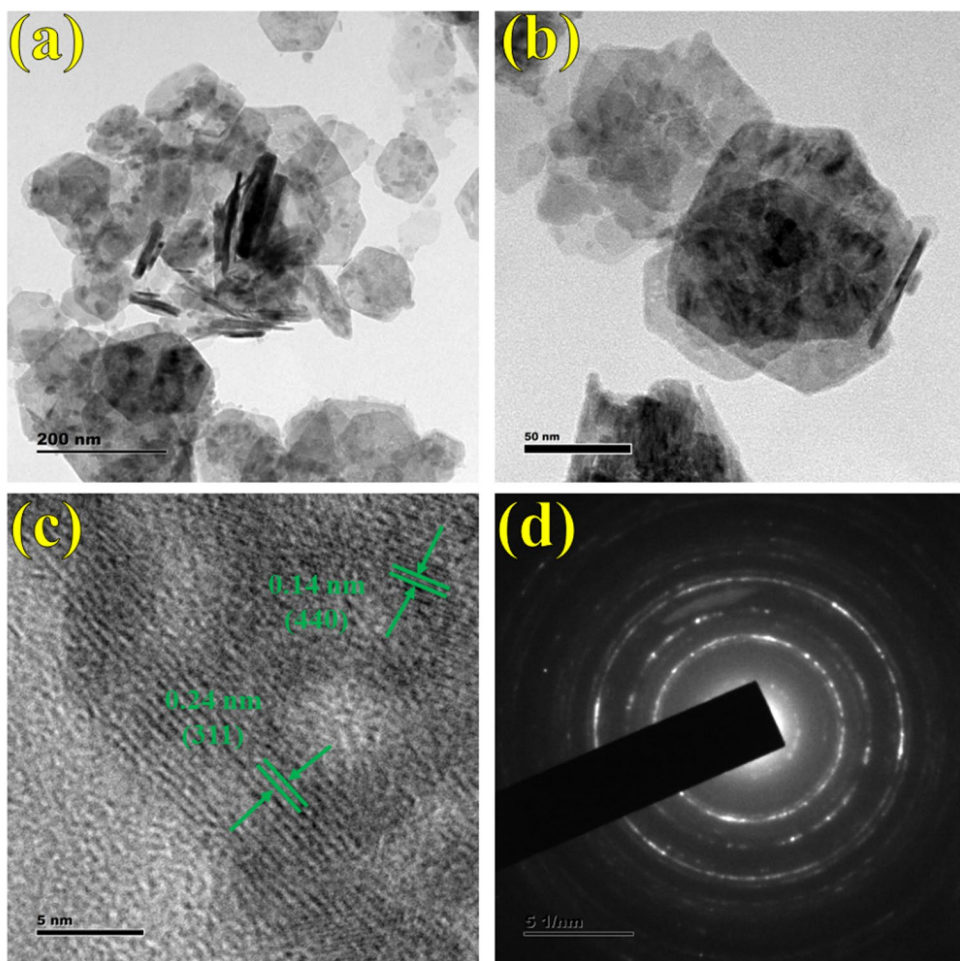
scan rates. As the scan rate rises, all the CV curves show a consistent shape profile with a constant increase of current density. Even when scanned at a rate of 100 mV s^{-1} , the CV curve maintains a pair of redox peaks, suggesting that this electrode material facilitates rapid redox reactions.

The peak potential shifts when the scan rate increases, which indicates that the electrode experiences minimal polarization. This can be attributed to the excellent electrical conductivity ensured by the morphologies of the electrode materials [5]. It's a well-known fact that the area beneath the CV curves directly correlates with the supercapacitor properties. To demonstrate the specific capacitance contribution of carbon black in the NiO, Co₃O₄, and NiCo₂O₄ electrodes, the carbon black electrodes were fabricated using 90% carbon black and 10% PVDF materials. The resultant carbon black CV is shown in Figure S1. The carbon black electrode provides a negligible amount of current density when compared to NiO, Co₃O₄, and NiCo₂O₄ electrodes. Among all the electrodes examined, the NiCo₂O₄ electrode exhibits a notably larger area beneath the CV curves, indicating

superior supercapacitive characteristics. This property can be attributed to the advantages of binary metal oxides as supercapacitor electrode materials, as both constituent metal ions play a role in expanding the range of feasible oxidation states and structures, thereby enhancing the electrode's performance.

The GCD measurements were carried out over a range of current densities, spanning from 1 to 20 A g^{-1} , to further assess the pseudocapacitive properties of the NiO, Co₃O₄, and NiCo₂O₄ electrodes synthesized in this study. The outcomes are depicted in Fig. 5d–f. The presence of plateaus in the charge–discharge profiles, occurring at approximately 0.3 V , indicates the typical pseudocapacitive behavior. This finding aligns well with the observations from the cyclic voltammetry (CV) curves. Among the electrodes, the NiCo₂O₄ demonstrates a longer discharge time, attributed to high supercapacitor characteristics. Using the GCD curves, the specific capacity (C g^{-1}) and specific capacitance (F g^{-1}) were estimated using the following Eqs. (6) and (7), respectively [30]:

Fig. 4 TEM analysis **a, b** Lower and higher magnification images, **c** fringes, and **d** SAED pattern of NiCo₂O₄ material



$$\text{Specific capacity} = \frac{I \times \Delta t}{m}, \tag{6}$$

$$\text{Specific capacitance} = \frac{I \times \Delta t}{m \times \Delta V} \tag{7}$$

where *I*, Δt , *m*, and ΔV represent the input current density (A g⁻¹), discharge time (s) from GCD profiles, weight of the active material (g), and the applied potential window, respectively. It is interesting to note that the NiO, Co₃O₄, and NiCo₂O₄ electrodes deliver the specific capacity of 150 C g⁻¹ (300 F g⁻¹), 251 C g⁻¹ (502 F g⁻¹), and 347 C g⁻¹ (694 F g⁻¹) respectively at a current density of 1 A g⁻¹. Remarkably, the specific capacity values achieved with the NiCo₂O₄ electrode surpass those previously reported for NiO, Co₃O₄, and NiCo₂O₄ and its composite-based electrode materials, as indicated in Table 1.

The outstanding performance of the NiCo₂O₄ electrode can be attributed to several key factors: (i) The small 1D nanorod and 2D nanoflake exhibit a thin structure and a high specific surface area, which offers a wide area for the electrochemical process, facilitating the supercapacitor

characteristics. (ii) This distinctive structure creates a pathway for rapid movement of electrolyte ions at the interface between electrode and electrolyte. This enhances the usage of the electrode materials during electrochemical analysis and outcomes in enhanced specific capacity properties. (iii) Both the 1D and 2D morphologies serve as spacer materials between them, effectively preventing the aggregation process during electrochemical reactions. This unique behavior ensures that all the reaction centers of the electrode materials remain easily available to alkali electrolyte ions, thereby enhancing specific capacity characteristics during GCD analysis.

The graph in Fig. 5g illustrates the relationship between specific capacity and current density. Notably, the specific capacity of electrodes exhibits a decrease as the current density increases, ranging from 1 to 20 mV s⁻¹. At lower current densities, the OH⁻ can effectively meet all the available electrode materials, enabling redox reactions to take place in the outer and inner surface area of the electrode materials. This contributes to the enhancement of the specific capacity of the electrodes. Conversely, at higher current densities, there is a reduced possibility of fully

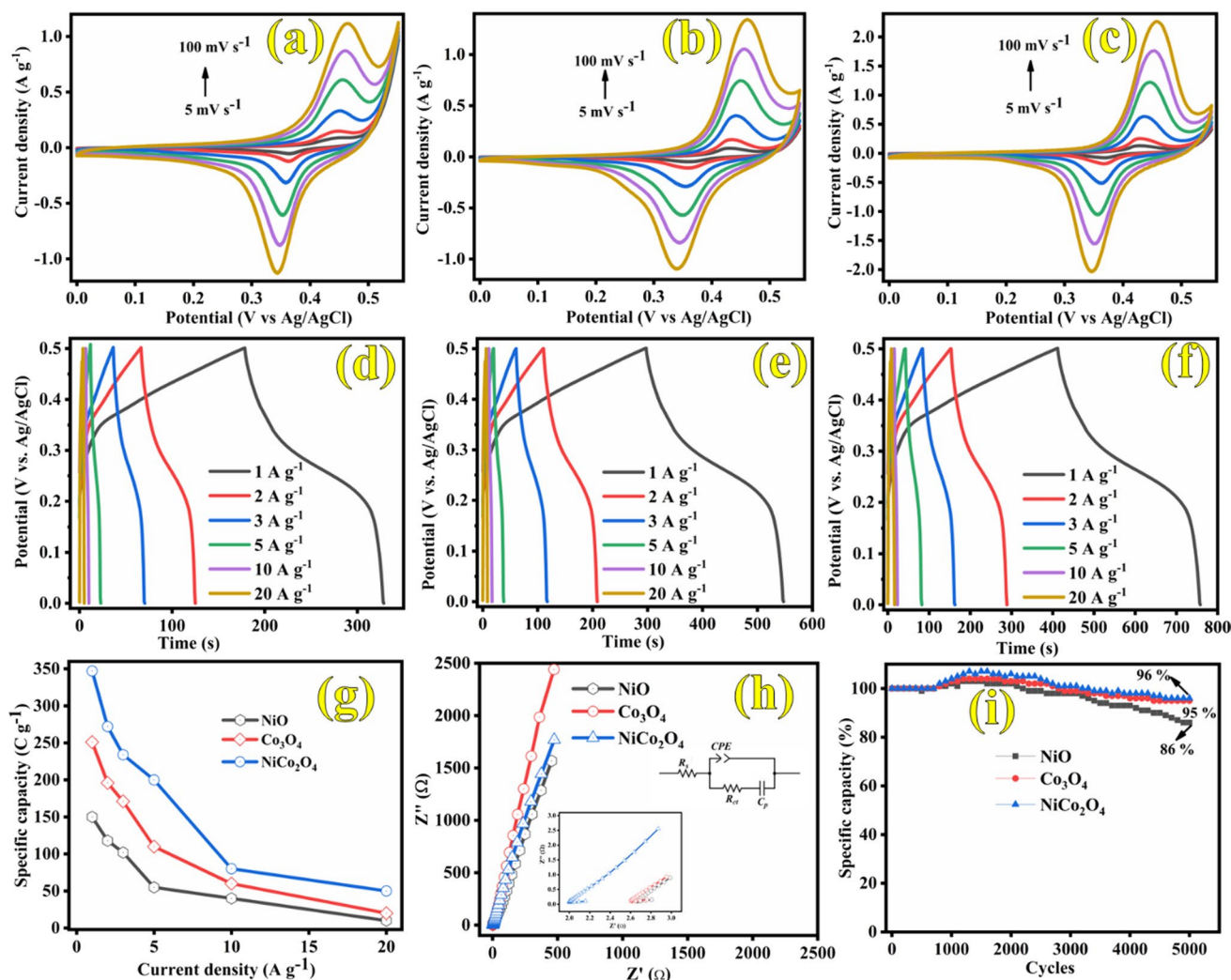


Fig. 5 CV curves of **a** NiO, **b** Co₃O₄, and **c** NiCo₂O₄ materials. GCD curves of **d** NiO, **e** Co₃O₄, and **f** NiCo₂O₄ materials. **g** Specific capacity vs current density, **h** impedance spectroscopy; (inset) zoom plot and equivalent circuit and **i** cyclic stability analysis of NiO, Co₃O₄ and NiCo₂O₄ materials

Table 1 Comparison performance table for supercapacitor properties

S. No	Materials	Electrolyte	Performance	References
1	NiCo ₂ O ₄ nanorods	2 M KOH	440 F g ⁻¹ at 5 mV s ⁻¹	[31]
2	NiCo ₂ O ₄ flowerlike structure	6 M KOH	658 F g ⁻¹ at 1 A g ⁻¹	[32]
3	NiCo ₂ O ₄ thin film	1 M KOH	580 F g ⁻¹ at 0.5 A g ⁻¹	[33]
4	NiCo ₂ O ₄ nanosheets@hollow microrod arrays	1 M KOH	678 F g ⁻¹ at 6 A g ⁻¹	[34]
5	Zn, Mn Co-Doped NiCo ₂ O ₄	1 M KOH	513.171 F g ⁻¹ at 10 mV s ⁻¹	[35]
6	NiCo ₂ O ₄ nanoplates	2 M KOH	332 F g ⁻¹ at 5 mV s ⁻¹	[36]
7	NiCo ₂ O ₄ nanomorphs	1 M Na ₂ SO ₄	479 F g ⁻¹ at 5 mV s ⁻¹	[37]
8	NiCo ₂ O ₄ -decorated porous carbon nanosheets	6 M KOH	596.8 F g ⁻¹ at 2 A g ⁻¹	[38]
9	NiCo ₂ O ₄ nanostructures	1 M Na ₂ SO ₄	415 F g ⁻¹ at 2 mV s ⁻¹	[39]
10	1D/2D NiCo ₂ O ₄	6 M KOH	347 C g ⁻¹ (694 F g ⁻¹) at 1 A g ⁻¹	Present work

employing all the electrode materials, resulting in redox reactions primarily taking place on the outer surface of the electrode materials. This tendency decreases the specific capacity at high current densities [40]. The EIS measurements were conducted to acquire a deeper understanding of the internal resistance and capacitive characteristics of the NiO, Co₃O₄, and NiCo₂O₄ electrodes. The corresponding Nyquist plots, along with the equivalent electrical circuit, are presented in Fig. 5h. Each Nyquist plot exhibited two distinct components: the semi-circle appeared in the high-frequency region and the straight line in the low-frequency region. The diameter of the semicircle within the Nyquist plot signifies the charge transfer resistance (R_{ct}), primarily arising from the charge transfer properties occurring at the electrode/ electrolyte interface [41]. The intercept value with the X axis at the high-frequency region corresponds to the equivalent series resistance (R_s), which comprises electrolyte resistance, intrinsic resistance, and interface contact resistance [42]. The R_s, R_{ct}, CPE, and C_p values from equivalent circuits were provided in Table S1. It is interesting to note that the NiCo₂O₄ electrode provides low R_{ct} and R_s values and high CPE and C_p values when compared to NiO, and Co₃O₄ electrodes, indicating the excellent supercapacitor property of the NiCo₂O₄ material. Cycling stability is another crucial metric for assessing the performance and quality of an electrode material. Figure 5i illustrates the cycling performance of the NiO, Co₃O₄, and NiCo₂O₄ electrodes, conducted at a current density of 10 A g⁻¹. At initial cycles, the specific capacity increases due to the activation of electrode materials [43]. After the activation process, slowly decreasing the specific capacity and attained 86, 95, and 96% of initial capacity respectively at the 5000th cycle. Among all the electrodes, the NiO electrode undergoes serious capacity decay due to the aggregated morphology. Within the NiCo₂O₄ electrode, the distinctive 1D nanorod morphology effectively prevents the restacking tendencies observed in the 2D nanoflake structure. This ensures that all the reaction centers of the electrode material remain accessible to electrolyte ions, contributing to excellent cyclic stability. Consequently, the results presented above demonstrate that NiCo₂O₄ exhibits remarkable electrochemical properties, including a commendable specific capacity, low resistance characteristics, and cycling stability. As a result, an asymmetric device was fabricated utilizing NiCo₂O₄ as the material of choice. The kinetic analysis has been conducted to differentiate between the diffusion-controlled and the surface-controlled properties as presented in Fig. 6. In general, the faradaic mode encompasses both diffusion-controlled faradaic behavior arising from conversion and alloying reactions, as well as redox pseudocapacitive processes involving charge transfer with surface/subsurface atoms. As evident from Fig. 5d–f,

a distinct plateau is noticeable in the GCD curves and this observation suggests that the energy storage mechanism in the NiO, Co₃O₄, and NiCo₂O₄ are not characterized by a pseudocapacitive process but rather exhibits a more diffusion-controlled battery property. In theory, the relationship between current density and the scan rate, *v*, is described by the following Eq. (8) and Fig. 6a–c [44].

$$i = av^b \quad (8)$$

where *a* and *i* represent a constant, and the measured current. When the value of *b* is 0.5, it signifies that the redox process is governed by a semi-infinite linear diffusion or diffusion-controlled process, while a *b* value of 1 indicates the surface-controlled reaction. The NiO, Co₃O₄, and NiCo₂O₄ provide the anodic *b*-values of 0.65, 0.6, and 0.54, whereas the cathodic *b*-values of 0.61, 0.58, and 0.52 respectively. These resultant values demonstrate that the dominated diffusion-controlled process in all electrode materials.

The current response (*i*) at a specific potential (*V*) can be expressed as the summation of capacitive effects *k*₁*v* and diffusion-controlled reactions *k*₂*v*^{1/2} following the following Eq. (9) [45].

$$i(V) = k_1v + k_2v^{1/2} \quad (9)$$

The values of *k*₁ and *k*₂ can be established by utilizing CV currents at various scan rates. By determining these *k*₁ and *k*₂ constants, it becomes possible to distinguish the proportion of current originating from surface capacitance and diffusion-controlled processes. Figures 6d–f show the percentage diffusion-controlled (purple-shaded) and surface-controlled (brown-shaded) processes at a scan rate of 10 mV s⁻¹ and Figs. 6g–i represent diffusion-controlled and surface controlled processes at all scan rates for NiO, Co₃O₄ and NiCo₂O₄ electrodes respectively. At a scan rate of 5 mV s⁻¹, the NiO, Co₃O₄, and NiCo₂O₄ electrodes provide 62, 81, and 87% of the diffusion-controlled process, whereas the 38, 19, and 13% of the surface-controlled process respectively. These findings illustrate that all the materials store a substantial amount of charge through diffusion-controlled processes during electrochemical analysis. In a two-electrode setup, an asymmetric supercapacitor (ASC) was fabricated using a positive electrode made from NiCo₂O₄ on Ni foam and a negative electrode utilizing an activated carbon (AC) electrode. A piece of cellulose membrane dipped in PVA/KOH (6 M) electrolyte and thus was placed between them to serve as the separator. The AC electrode was fabricated using the same method as the NiCo₂O₄ electrode, with the exclusion that AC was utilized as the electrode substance. The charge balance theory (*Q*⁺ = *Q*⁻) was utilized for the mass ratio (*m*⁺/*m*⁻) of positive and negative electrodes. The mass ratio is 0.34 based on the Eq. (10) [46].

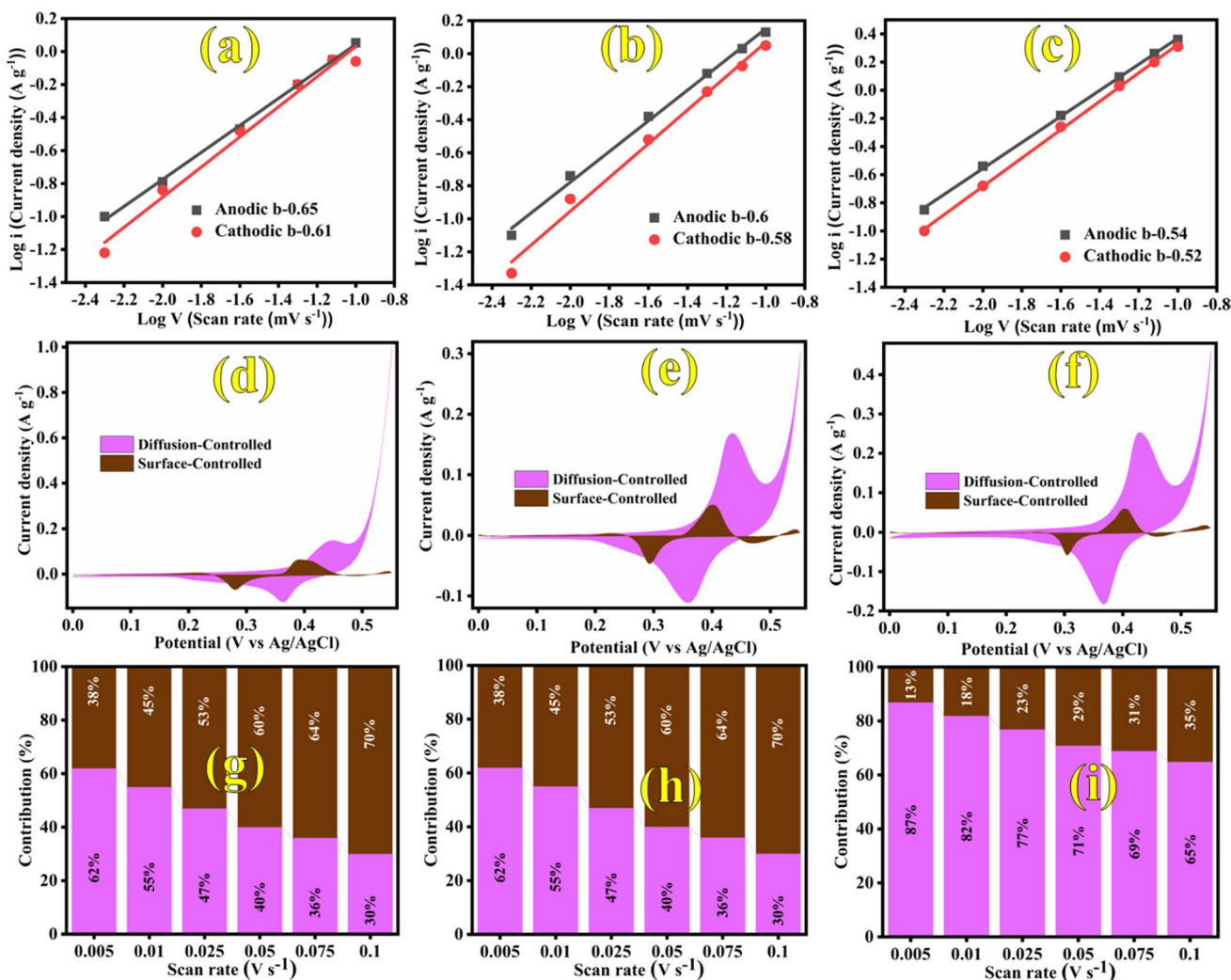


Fig. 6 Logarithmic plots of **a** NiO, **b** Co₃O₄, and **c** NiCo₂O₄ materials. Capacitive and diffusive contribution (at 10 mV s⁻¹) of **d** NiO, **e** Co₃O₄, and **f** NiCo₂O₄ materials. Capacitive and diffusive contribu-

tion to the total capacitance at various scan rates for **g** NiO, **h** Co₃O₄, and **i** NiCo₂O₄ materials

$$\frac{m_{(cathode)}}{m_{(anode)}} = \frac{(C \times \Delta V)_{(anode)}}{(C \times \Delta V)_{(cathode)}} \tag{10}$$

where C, V, and m denote the specific capacity, voltage window, and weight of the electroactive material. Figure 7a shows the CV curves anode and cathode at a scan rate of 50 mV s⁻¹ in 6 M KOH electrolyte. The absence of redox peaks in the CV curve of the AC electrode indicates the predominance of the electrochemical double-layer charge storage mechanism. Figure 7b shows the CV curves of the NiCo₂O₄//AC asymmetric device with various voltage windows. However, a minor hump was noticeable within the voltage range of 1.6–1.8 V, indicating the occurrence of the oxygen evolution reaction on the positive electrode.

Consequently, the appropriate working voltage window for the NiCo₂O₄//AC device was determined to be 1.6 V.

When the scan rates varied from 5 to 100 mV s⁻¹, the area under the CV curve gradually expanded without significant distortion in its shape (as shown in Fig. 7c). This observation signifies excellent reversibility for rapid charge/discharge processes, which is further demonstrated by the quasi-symmetric GCD curves displayed in Fig. 7d. The NiCo₂O₄//AC device delivers an impressive specific capacity of 141 C g⁻¹ (88.1 F g⁻¹) at a current density of 1 A g⁻¹. Energy and power density characteristics are pivotal parameters in the context of supercapacitor applications and are thus calculated using Eqs. (11) and (12) respectively.

$$E_{cell} = \frac{1}{2 \times 3.6} \times C_{sp} \times \Delta V^2, \tag{11}$$

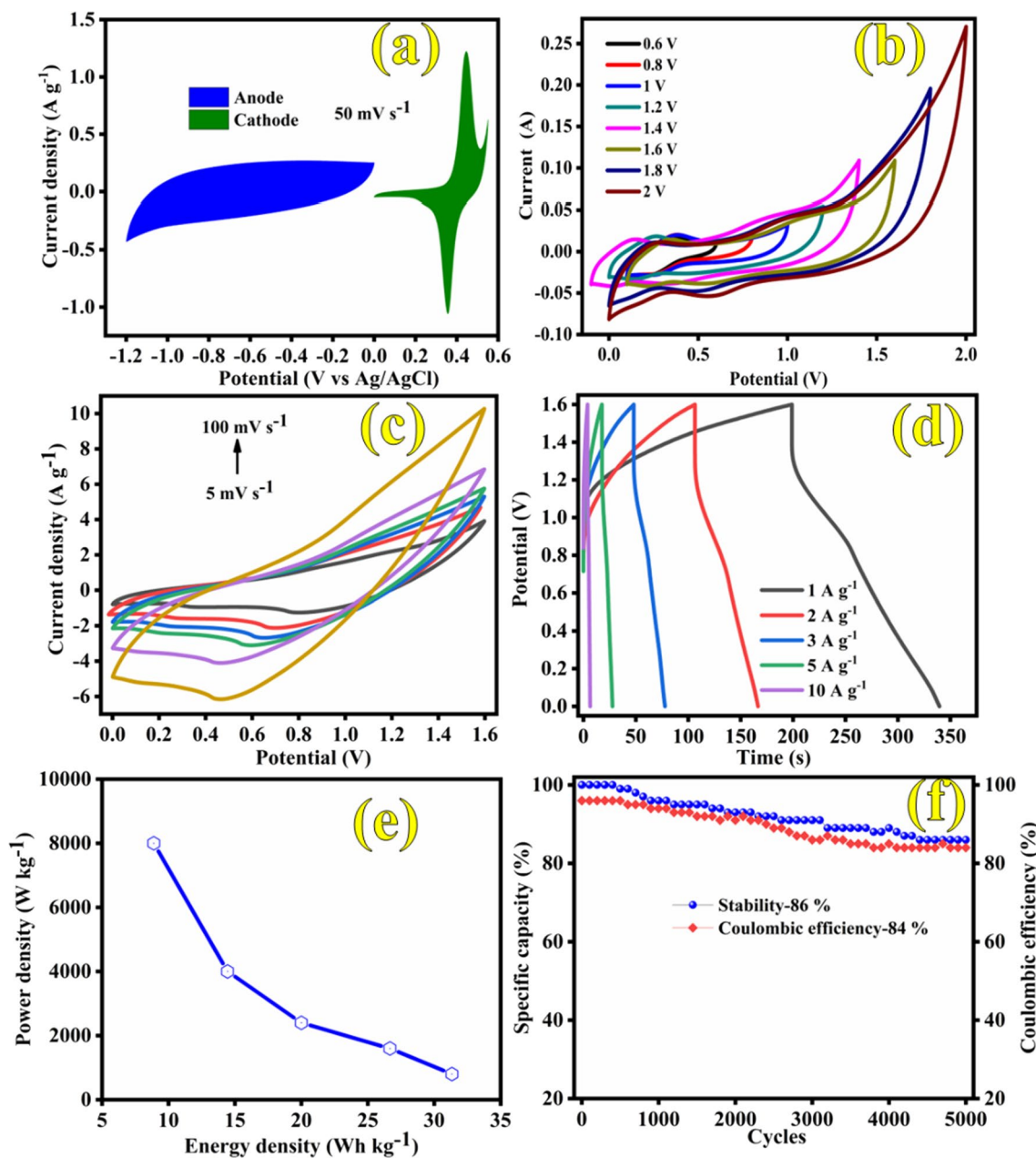


Fig. 7 NiCo₂O₄//AC device analysis. **a** CV curves of AC and NiCo₂O₄ at a scan rate of 50 mV s⁻¹, **b** CV curves with different voltage windows, **c** CV curves with different scan rates, **d** GCD analysis, **e** Ragone plot and **f** cyclic stability and coulombic efficiency analyses

$$P_{cell} = \frac{3600 \times E_{cell}}{\Delta t}, \tag{12}$$

where *C_{sp}*, *ΔV*, and *Δt* represent the specific capacity (C g⁻¹), current density (A g⁻¹), and discharge time (s) respectively. The Ragone plot Fig. 7e provides information about the energy and power density properties. The NiCo₂O₄//AC device provides the energy and power density of 31.3 Wh kg⁻¹ and 800 Wh kg⁻¹ respectively at a current density of 1 A g⁻¹. The cyclic stability and coulombic efficiency analyses

were done and shown in Fig. 7f. The NiCo₂O₄//AC device exhibited admirable cycling stability, retaining 86% of its initial capacitance even after undergoing 5000 GCD cycles at a current density of 10 A g⁻¹. Coulombic efficiency is a critical factor that signifies the stability of electrode materials during the charge–discharge process. The calculation of the coulombic efficiency for an electrode is determined using the following Eq. (13):

$$\eta = \frac{t_d}{t_c} \times 100 \quad (13)$$

where t_d is discharge time (s) and t_c is charging time (s). At an initial cycle, the NiCo₂O₄//AC device provides 96% of coulombic efficiency, and 84% of initial coulombic efficiency is retained after 5000 GCD cycles at a current density of 10 A g⁻¹. Hence, the 1D nanorod and 2D nanoflake morphologies of NiCo₂O₄ material have exhibited significant potential in the field of energy storage applications.

4 Conclusion

In summary, this work progressed a simple approach for the fabrication of 1D nanorod and 2D nanoflake morphologies NiCo₂O₄ material for the asymmetric supercapacitor application. The distinctive mixed nanostructure not only promoted efficient electron transfer and ions adsorption/desorption but also substantially augmented the number of electroactive sites while safeguarding the structural integrity of the electrode material. Consequently, the NiCo₂O₄ material follows the diffusion-controlled process and thus enhances the supercapacitor performance. In three electrode systems, the NiCo₂O₄ delivers the specific capacity of 347 C g⁻¹ (694 F g⁻¹) at 1 A g⁻¹ with excellent cyclic stability and 96% of initial capacity retention at 5000 cycles at 10 A g⁻¹. The ASC device renders the specific capacity of 141 C g⁻¹ (88 F g⁻¹) at 1 A g⁻¹, with an excellent energy and power density of 31.3 Wh kg⁻¹ and 800 W kg⁻¹ respectively. Due to the advanced mixed morphologies, the device withstands 86% capacity retention after 5000 GCD cycles at 10 A g⁻¹. Hence, this study offers an effective approach for designing efficient electrodes featuring both 1D and 2D morphologies, catering to the high-performance demands of energy storage devices.

Supplementary Information The online version contains supplementary material available at <https://doi.org/10.1007/s00339-024-07439-1>.

Author contributions M. Sathiyaseelan: Formal analysis, Investigation, Writing—original draft. Lakshmi Kunhikrishnan: Formal analysis, Investigation. P. Jacqueline Rosy: Formal analysis, Investigation. G. Sivashanmugam: Conceptualization, Methodology, Writing—original draft. B. Preethi: Conceptualization, Methodology, Writing—original draft, Writing—review & editing.

Funding The authors declare they have no financial interests.

Data availability The authors declare that the data supporting the findings of this study are available within the paper. Should any raw data files be needed in another format they are available from the corresponding author upon reasonable request.

Declarations

Conflict of interest The authors declare that they have no known competing financial interests or personal relationships that could have appeared to influence the work reported in this paper.

References

1. P. Simon, Y. Gogotsi, B. Dunn, *Science* **343**, 1210 (2014)
2. P. Simon, Y. Gogotsi, *Nat. Mater.* **7**, 845 (2008)
3. G. Sivashanmugam, K. Lakshmi, B. Preethi, S. Nelson, M. Sathiyaseelan, *J. Mater. Sci. Mater. Electron.* **32**, 27148 (2021)
4. L. Kunhikrishnan, R. Shanmugham, G. Sivashanmugam, *J. Solid State Electrochem.* **25**, 1 (2021)
5. C. Yuan, J. Li, L. Hou, X. Zhang, L. Shen, X.W. Lou, *Adv. Funct. Mater.* **22**, 4592 (2012)
6. B. E. Convey, *Electrochemical Supercapacitors: Scientific Fundamentals and Technological Applications* (Springer science & business media, 2013)
7. B.Y. Chang, E. Ahn, S.M. Park, *J. Phys. Chem. C* **112**, 16902 (2008)
8. D. Rochefort, A.L. Pont, *Electrochem. Commun.* **8**, 1539 (2006)
9. Y. Liu, S.P. Jiang, Z. Shao, *Mater. Today Adv.* **7**, 100072 (2020)
10. M.B. Sassin, C.N. Chervin, D.R. Rolison, J.W. Long, *Acc. Chem. Res.* **46**, 1062 (2013)
11. X. Xia, J. Tu, Y. Zhang, X. Wang, C. Gu, X.B. Zhao, H.J. Fan, *ACS Nano* **6**, 5531 (2012)
12. M. Guan, Q. Wang, X. Zhang, J. Bao, X. Gong, Y. Liu, *Front. Chem.* **8**, 1 (2020)
13. J. Sun, L. Guo, X. Sun, J. Zhang, L. Hou, L. Li, S. Yang, C. Yuan, *Batter. Supercaps* **2**, 820 (2019)
14. S. Chen, W. Xing, J. Duan, X. Hu, S.Z. Qiao, *J. Mater. Chem. A* **1**, 2941 (2013)
15. S. Deka, *Dalt. Trans.* **52**, 839 (2022)
16. C. Wang, E. Zhou, W. He, X. Deng, J. Huang, M. Ding, X. Wei, X. Liu, X. Xu, *Nanomaterials* **7**, 1 (2017)
17. Y. Li, X. Han, T. Yi, Y. He, X. Li, *J. Energy Chem.* **31**, 54 (2019)
18. E. Mackiewicz, T. Wejrzanowski, R. Nowacki, J. Jaroszewicz, J. Marchewka, Ł. Wilk, P. Bezkosty, M. Sitarz, *Appl. Mater. Today* **33**, 101859 (2023)
19. X. Liu, Q. Long, C. Jiang, B. Zhan, C. Li, S. Liu, Q. Zhao, W. Huang, X. Dong, *Nanoscale* **5**, 6525 (2013)
20. L. Han, X.Y. Yu, X.W. David Lou, *Adv. Mater.* **28**, 4601 (2016)
21. G. Li, H. Cai, X. Li, J. Zhang, D. Zhang, Y. Yang, J. Xiong, *A.C.S. Appl. Mater. Interfaces* **11**, 37675 (2019)
22. H. Rong, T. Chen, R. Shi, Y. Zhang, Z. Wang, *ACS Omega* **3**, 5634 (2018)
23. J. Yesuraj, J. Kim, R. Yang, K. Kim, *A.C.S. Appl. Energy Mater.* **5**, 10149 (2022)
24. V. Selvanathan, M. Shahinuzzaman, S. Selvanathan, D.K. Sarkar, N. Algethami, H.I. Alkhamash, F.H. Anuar, Z. Zainuddin, M. Aminuzzaman, H. Abdullah, M. Akhtaruzzaman, *Catalysts* **11**, 1523 (2021)
25. J. Yesuraj, H.O. Lee, M. Kumar Pandiyan, J. Jayavelu, M. Bhagavathiachari, K. Kim, *J. Mol. Struct.* **1256**, 132999 (2022)
26. H.-B. Jang, K. Ryeol Park, K. Min Kim, S.-K. Hyun, J.-E. Jeon, Y. Sik Song, S.-K. Park, K. Moon, C. Ahn, S.-C. Lim, J. Lee, J. Cheol Kim, H. Han, S. Mhin, *Nanomaterials* **11**, 55 (2021)
27. G. Anandha Babu, G. Ravi, T. Mahalingam, M. Kumaresavanji, Y. Hayakawa, *Dalt. Trans.* **44**, 4485 (2015)
28. H. Wang, Q. Gao, L. Jiang, *Small* **7**, 2454 (2011)
29. H. Fu, Y. Liu, L. Chen, Y. Shi, W. Kong, J. Hou, F. Yu, T. Wei, H. Wang, X. Guo, *Electrochim. Acta* **296**, 719 (2019)
30. J. Yesuraj, K. Kim, *J. Energy Storage* **58**, 106315 (2023)

31. M. Sethi, D.K. Bhat, J. Alloys Compd. **781**, 1013 (2019)
32. H. Chen, J. Jiang, L. Zhang, T. Qi, D. Xia, H. Wan, J. Power. Sources **248**, 28 (2014)
33. V. Gupta, S. Gupta, N. Miura, J. Power. Sources **195**, 3757 (2010)
34. X.F. Lu, D.J. Wu, R.Z. Li, Q. Li, S.H. Ye, Y.X. Tong, G.R. Li, J. Mater. Chem. A **2**, 4706 (2014)
35. S.S. Pradeepa, P. Rajkumar, K. Diwakar, K. Sutharthani, R. Subadevi, M. Sivakumar, ChemistrySelect **6**, 6851 (2021)
36. T. Kim, A. Ramadoss, B. Saravanakumar, G.K. Veerasubramani, S.J. Kim, Appl. Surf. Sci. **370**, 452 (2016)
37. S.J. Uke, G.N. Chaudhari, A.B. Bodade, S.P. Mardikar, Mater. Sci. Energy Technol. **3**, 289 (2020)
38. V. Veeramani, R. Madhu, S.M. Chen, M. Sivakumar, C. Te Hung, N. Miyamoto, S. Bin Liu, Electrochim. Acta **247**, 288 (2017)
39. A.K.N. Ananta Sasmal, J. Energy Storage **58**, 106342 (2023)
40. R.J. Deokate, R.S. Kalubarme, C.J. Park, C.D. Lokhande, Electrochim. Acta **224**, 378 (2017)
41. D. Cai, S. Xiao, D. Wang, B. Liu, L. Wang, Y. Liu, H. Li, Y. Wang, Q. Li, T. Wang, Electrochim. Acta **142**, 118 (2014)
42. T.H. Ko, D. Lei, S. Balasubramaniam, M.K. Seo, Y.S. Chung, H.Y. Kim, B.S. Kim, Electrochim. Acta **247**, 524 (2017)
43. J. Yesuraj, S.A. Suthanthiraraj, J. Mol. Struct. **1181**, 131 (2019)
44. B.K. Lesel, J.S. Ko, B. Dunn, S.H. Tolbert, ACS Nano **10**, 7572 (2016)
45. D. Chao, C. Zhu, P. Yang, X. Xia, J. Liu, J. Wang, X. Fan, S.V. Savilov, J. Lin, H.J. Fan, Z.X. Shen, Nat. Commun. **7**, 1 (2016)
46. J. Zhao, Y. Wang, Y. Qian, H. Jin, X. Tang, Z. Huang, J. Lou, Q. Zhang, Y. Lei, and S. Wang, Adv. Funct. Mater. **33**, (2023)

Publisher's Note Springer Nature remains neutral with regard to jurisdictional claims in published maps and institutional affiliations.

Springer Nature or its licensor (e.g. a society or other partner) holds exclusive rights to this article under a publishing agreement with the author(s) or other rightsholder(s); author self-archiving of the accepted manuscript version of this article is solely governed by the terms of such publishing agreement and applicable law.